Published in final edited form as:
Metab Eng. 2011 November ; 13(6): 656–665. doi:10.1016/j.ymben.2011.08.002.

Mapping photoautotrophic metabolism with isotopically nonstationary ^{13}C flux analysis

Jamey D. Young[1,*], **Avantika A. Shastri**[2,*], **Gregory Stephanopoulos**[3,†], and **John A. Morgan**[2,†]

[1]Department of Chemical and Biomolecular Engineering, Vanderbilt University, Nashville, TN 37235, USA

[2]School of Chemical Engineering, Purdue University, West Lafayette, IN 47907, USA

[3]Department of Chemical Engineering, Massachusetts Institute of Technology, Cambridge, MA 02139, USA

Abstract

Understanding *in vivo* regulation of photoautotrophic metabolism is important for identifying strategies to improve photosynthetic efficiency or re-route carbon fluxes to desirable end products. We have developed an approach to reconstruct comprehensive flux maps of photoautotrophic metabolism by computational analysis of dynamic isotope labeling measurements and have applied it to determine metabolic pathway fluxes in the cyanobacterium *Synechocystis* sp. PCC6803. Comparison to a theoretically predicted flux map revealed inefficiencies in photosynthesis due to oxidative pentose phosphate pathway and malic enzyme activity, despite negligible photorespiration. This approach has potential to fill important gaps in our understanding of how carbon and energy flows are systemically regulated in cyanobacteria, plants, and algae.

Keywords

metabolic flux analysis; cyanobacteria; isotopomer analysis; mass spectrometry; photoautotrophic metabolism; carbon fixation

1. INTRODUCTION

Photoautotrophic metabolism is the process by which plants, algae, and other photosynthetic organisms use light energy to fix carbon dioxide into complex organic molecules. This represents the primary source of all food on earth as well as raw materials for bio-based production of fuels and chemicals. To date, six different pathways of carbon fixation have been identified in nature (Berg et al., 2010), of which the Calvin-Benson-Bassham (CBB)

†To whom correspondence should be addressed. gregstep@mit.edu; jamorgan@purdue.edu.
*These authors contributed equally to this work.

AUTHOR CONTRIBUTIONS

JDY designed the experiment and flux calculation method, analyzed the data and wrote the manuscript. AAS designed and performed the experiment, analyzed the data and wrote the manuscript. GS designed the flux calculation method and wrote the manuscript. JAM designed the experiment, analyzed the data and wrote the manuscript.

cycle accounts for more than 99% of global primary biomass production (Overmann and Garcia-Pichel, 2006). Over one-third of this production is attributable to prokaryotic carbon fixation, mainly by marine cyanobacteria. Several groups have recently demonstrated the feasibility of engineering cyanobacteria to convert solar energy and atmospheric CO_2 directly into biofuels (Atsumi et al., 2009; Dutta et al., 2005; Lindberg et al., 2010; Liu et al., 2011), thus providing a potential strategy to harness their vast photosynthetic capacity toward meeting global energy demands while transitioning to a carbon-neutral society. Despite these advances, the productivities achieved by cyanobacterial fermentations are currently too low for industrial feasibility (Sheehan, 2009), and few tools have been developed that specifically address the challenges of redirecting or enhancing metabolic flux in photosynthetic organisms. Furthermore, it has been estimated that less than 1% of the available solar energy flux is converted into chemical energy by photosynthetic processes (Overmann and Garcia-Pichel, 2006), and developing strategies to enhance the efficiency of photosynthetic carbon fixation is a key step toward solving food, energy, and environmental challenges of the future.

The ability to quantitatively map intracellular carbon fluxes using isotope tracers and metabolic flux analysis (MFA) is critical for identifying pathway bottlenecks and elucidating network regulation in biological systems, especially those that have been engineered to alter their native metabolic capacities (Sauer, 2006). Although ^{13}C is the preferred isotope tracer for mapping central carbon metabolism in heterotrophic organisms, photoautotrophs assimilate carbon solely from CO_2 and therefore produce a uniform steady-state ^{13}C-labeling pattern that is insensitive to fluxes (Fig. 1). Thus, conventional *steady-state* ^{13}C-MFA is incapable of quantifying autotrophic metabolic fluxes (Shastri and Morgan, 2007). As a result, prior ^{13}C-MFA studies of plants (Schwender, 2008) and cyanobacteria (Yang et al., 2002) have been limited to heterotrophic (HT) or mixotrophic (MT) growth conditions, typically with sugar as the major carbon source. To overcome this limitation, we hypothesized that *transient* measurements of isotope incorporation following a step change from unlabeled to labeled CO_2 could be used to map carbon fluxes under photoautotrophic (PA) growth conditions. This involves quantification of intracellular metabolic fluxes based upon computational analysis of dynamic isotope labeling trajectories, an approach that has been called isotopically nonstationary MFA (INST-MFA) (Wiechert and Noh, 2005). An underlying assumption of this approach is that metabolic fluxes and pool sizes remain constant throughout the labeling experiment and are not perturbed by the introduction of ^{13}C tracer. If this assumption is valid, a single set of flux and pool size parameters (along with their associated uncertainties) can be estimated that is consistent with all transient isotopomer measurements obtained during the experiment. We have recently introduced computational routines that achieve more than 5000-fold speedup relative to previous INST-MFA algorithms (Young et al., 2008), which now makes this approach computationally feasible for autotrophic networks of realistic size. The aim of this contribution, therefore, was to apply these computational tools along with state-of-the-art mass spectrometry approaches to produce a comprehensive photoautotrophic flux map of a model photosynthetic organism.

2. MATERIALS AND METHODS

2.1. Strain and cultivation conditions

Synechocystis sp. PCC 6803 was obtained from ATCC (ATCC # 27150) and cultured in a 1.25 L bioreactor (Bioflo 3000, New Brunswick Scientific, NJ) on BG-11 medium buffered with 10 mM HEPES. Air was supplied at 1–1.5 L/min, and the reactor was stirred at 350 rpm. Temperature was controlled at 30°C and pH was maintained in the range 8.0–8.5 by automatic addition of 2 N H_2SO_4. Nine 23 W cool white fluorescent lights (Sylvania, MA) provided an average surface light flux of 400 $\mu E/m^2/s$. Only 5 lights were turned on in the

initial 12 hours of growth in order to prevent photoinhibition. The outlet gas CO_2 concentration was monitored using a LI-820 CO_2 gas analyzer with 14 cm optical bench (LI-COR Biosciences, NE).

2.2. Sample removal and metabolite extraction

The sideport of the standard reactor vessel was sealed with a thick autoclavable membrane. A two-way luer stopcock (Popper and Sons, NY) with an extremely small holdup volume (< 0.5 mL) was fitted with a gauge 16 needle and inserted into the reactor via the membrane. A short piece of tubing was attached to the end of the stopcock, which allowed the rapid fitting of a syringe. This enabled repeated withdrawal of 20 mL samples into 60 mL syringes (BD Biosciences, MD) containing 40 mL of quenching solution (60% methanol in water) precooled to −40°C or lower. Each sample took less than 3 seconds to withdraw. The contents of each syringe were rapidly transferred to 50 mL centrifuge tubes that were kept in a −20°C bath. Using this procedure, samples of 20 mL size could be withdrawn reliably every 20 seconds. Each quenched sample was centrifuged for 10 minutes at 8000g and −20°C. The supernatant was discarded and the cell pellet was extracted with 500 µL pure methanol, followed by two extractions with 500 µL of a 50/50 methanol-water solution. Each extraction was carried out for 30 minutes at a temperature below −20°C, and the extracts were pooled together and stored at −20°C.

2.3. Carbon labeling experiment

The labeling experiment was initialized when the cell density reached an OD_{730} of 0.6. A sample corresponding to time zero (unlabeled) was withdrawn from the sideport using a syringe. The aeration was then stopped and gas inlets and outlets to the reactor were rapidly clamped to prevent unlabeled CO_2 from entering the system. A 20 mL aliquot of 50% $NaH^{13}CO_3$ (Sigma, 98% isotopic purity) was injected swiftly into the system using a syringe, and 20 mL samples were withdrawn and rapidly quenched at time points of 20, 40, 60, 90, 130, 250, 480, and 610 seconds. Intracellular metabolites were obtained from these samples by solvent extraction of cell pellets. Additional samples were withdrawn without quenching and rapidly filtered through a syringe filter. These supernatants were used to identify metabolites secreted into the extracellular media. Metabolite samples were analyzed using a combination of GC-MS and LC-MS/MS to determine labeling and concentration of metabolites in both cell extracts and culture supernatants. Samples were also withdrawn for measurement of cell dry weight.

2.4. GC-MS measurement of metabolite labeling and concentration

The GC-MS method was adapted from Roessner et al. (2000) and was performed using an Agilent 6890N/5975B quadrupole GC-MS system. All samples were dried under vacuum at room temperature in a Centrivap (Labconco Corporation, MO). Ribitol was added as an internal standard to all the samples prior to the drying step to achieve a final concentration of 0.328 µM in the derivatized solution. The samples were subsequently methoximated with 50 µL of methoxyamine hydrochloride in pyridine (2mg/mL) for 90 minutes at 40°C. Next, 50µL BSTFA + 10% TMCS (Pierce Biotechnology, IL) was added to the reaction mixture and incubated at 40°C for 30 minutes. The derivatized samples remained for 6–12 hours at room temperature in a dessicator, to ensure complete reaction. All samples were run on the GC-MS within 30 hours of derivatization. An HP-5MS column of 180 µm diameter, 30 m length and 0.20 µm film thickness (Agilent Technologies, CA) was used with helium as the carrier gas. The total column flow was set to 1 mL/min, and 1 µL injections were made using a 230°C inlet temperature in splitless mode and a purge flow of 100 mL/min set to activate 1 min after injection. The column temperature was held at 70°C for 3 minutes, increased to 305°C at 3°C/min, and held at 305°C for 2 minutes. Spectra were recorded in the range of 50–600 m/z. Metabolites were identified by comparison to the retention time

and characteristic ions of pure standards. Linear calibration curves were prepared with purchased standards and used to quantify the metabolites in the samples. All chemicals were purchased from Sigma Aldrich, USA.

2.5. LC-MS/MS measurement of metabolite labeling and concentration

An ion-pairing LC-MS/MS method was adapted from Oldiges et al. (2004) and was performed on a Shimadzu SCL10 LC system coupled to a linear ion-trap triple quadrupole MS/MS system (4000 Q TRAP, AB Sciex Instruments) at the Proteomics and Mass Spectrometry Facility, Donald Danforth Center, St. Louis, MO. A Synergi Hydro-RP column (150mm × 2 mm, Phenomenex Inc, CA) was used with gradient elution. The eluents used were 10 mM tributylamine + 15 mM acetic acid (A) and methanol (B). In order to dissolve tributylamine completely in water, the tributylamine and acetic acid were first mixed together in a dry flask before the requisite amount of ultrapure water was added. The final pH of eluent A was found to be 4.5–4.6. All chemicals were HPLC or LC-MS grade and purchased from Sigma Aldrich, USA. The eluents were filtered before use. An injection volume of 10 μL was used, and the column flow and temperature were constant at 0.3 mL/min and 25°C, respectively. The gradient profile was as follows: 0% B (0 min), 8% B (8 min), 22% B (18 min), 40% B (28 min), 60% B (32 min), 90% B (34 min), 90% B (37 min), 0% B (39 min), 0% B (49 min). The acquisition of labeling and concentration data was performed using negative electrospray ionization in the multiple reaction monitoring (MRM) mode. The final parameters used for isotopomer measurements are listed in Supplementary Table I. All data acquisition and analysis was performed on the Analyst 4.1.2 software (AB/MDS Sciex) supplied with the instrument.

2.6. Isotopically nonstationary metabolic flux analysis (INST-MFA)

We applied our previously developed INST-MFA approach (Young et al., 2008) to estimate intracellular metabolic fluxes and metabolite pool sizes based on the measured isotope labeling dynamics of intracellular metabolites. This approach relies upon an elementary metabolite unit (EMU) decomposition of the underlying isotopomer network to efficiently simulate the effects of varying fluxes on the labeling state of measurable metabolites (Antoniewicz et al., 2007). Metabolic fluxes and pool sizes were estimated by minimizing the lack-of-fit between experimentally measured and computationally simulated mass isotopomer distributions (MIDs) using least-squares regression. All isotopic measurements used for flux determination are listed in Table I. The flux and pool size parameters of the isotopomer network model were iteratively adjusted using a Levenberg-Marquardt algorithm until optimal agreement with experimental data was obtained (Madsen et al., 2004). All results were subjected to a chi-square statistical test to assess goodness-of-fit, and accurate 95% confidence intervals were computed for all estimated parameters by evaluating the sensitivity of the sum-of-squared residuals to parameter variations (Antoniewicz et al., 2006).

A list of the reactions included in the isotopomer network model is provided in Supplementary Table II. (Refer to Supplementary Materials for a detailed description of the model formulation.) In total, the model was capable of fitting 921 independent mass isotopomer measurements using 224 adjustable parameters (34 free fluxes + 29 pool sizes + 161 measurement scaling factors). The measurement scaling factors were required to properly normalize the MIDs of each MS fragment ion (Mollney et al., 1999). The model required 559 ordinary differential equations (ODEs) to simulate the change in all measured MIDs over time. In addition, 35,217 ODEs were needed to compute sensitivities of these MIDs with respect to all adjustable parameters. Overall, the model consisted of 35,776 ODEs and required approximately 3 seconds to simulate using the best-fit parameters. To ensure that the final solution was the global optimum, flux estimation was repeated at least

50 times starting from random initial values. Supplementary Fig. 1 shows MID trajectories for all experimentally measured GC-MS and LC-MS/MS ions along with best-fit model simulations. The fit was statistically accepted based on a chi-square test of the sum-of-squared residuals (SSR), which was assessed at the 95% confidence level with 697 degrees of freedom (SSR = 684.7 versus the expected range [625.7, 772.1]). A full listing of the optimal parameter estimates can be found in Supplementary Tables III, IV and V.

3. RESULTS AND DISCUSSION

3.1. Carbon labeling experiment

To assess the capability of ^{13}C INST-MFA to quantify PA fluxes, we applied this approach to the cyanobacterium *Synechocystis* sp. PCC 6803 growing in a controlled photobioreactor environment with bicarbonate provided as the sole carbon source. (Bicarbonate equilibrates with dissolved CO_2 in the culture medium and therefore provides a convenient route to administer CO_2 to liquid cultures.) Following the introduction of ^{13}C-labeled bicarbonate to the bioreactor, a time-series of metabolite samples was obtained by rapid quenching and extraction of cyanobacterial cells. Dynamic changes in isotope labeling patterns of central carbon metabolites were quantified using both gas chromatography-mass spectrometry (GC-MS) and liquid chromatography-tandem mass spectrometry (LC-MS/MS), followed by computational analysis of these trajectories to estimate metabolic pathway fluxes using INST-MFA (Fig. 2). This is the first time, to our knowledge, that a comprehensive flux analysis has been performed based on isotope labeling data obtained from a fully autotrophic system.

The labeling dynamics of 21 fragment ions derived from 15 different central metabolites were measured over a 20-minute time window following tracer administration. As shown in Fig. 3A, the relative abundances of unlabeled (M0) mass isotopomers dropped rapidly at the outset of the labeling period due to the emergence of ^{13}C-enriched mass isotopomers (M1, M2, etc.). Initially, singly-labeled (M1) mass isotopomers accumulated due to incorporation of single ^{13}C atoms into previously unlabeled metabolites. These M1 mass isotopomers were gradually supplanted by M2, M3, and higher mass isotopomers as further ^{13}C atoms were incorporated, resulting in transient overshoots in M1 abundance. Note, however, that the average ^{13}C-enrichment of each metabolite increased monotonically over time despite the rise and fall of M1 mass isotopomers (Fig. 3B). Steady-state labeling was typically obtained in less than 10 minutes, with the notable exception of tricarboxylic acid (TCA) pathway intermediates (e.g., succinate, fumarate, citrate) that were more slowly labeled.

3.2. Secretion of organic metabolites

In addition to measurements of intracellular metabolite labeling, extracellular samples were collected for analysis of secreted metabolites. Glycolate was the only secreted metabolite that could be identified in the culture medium. The extracellular concentration of glycolate at the end of the 32-hour batch growth period was estimated to be less than 5μM. Based on this measurement and the final biomass concentration of 204 mg/L, we estimated that the carbon lost to glycolate was approximately 1000-fold less than the amount of carbon incorporated into biomass. Therefore, we concluded that secretion of organic metabolites by *Synechocystis* was essentially negligible under photoautotrophic conditions, and that all fixed carbon was either incorporated into biomass or released as CO_2 due to oxidative processes. As a result, we were able to apply INST-MFA based solely on the intracellular metabolite labeling data while normalizing all flux values to the net rate of CO_2 conversion into biomass (Fig. 4). This rate was estimated from the growth rate and carbon content of the culture, which was 0.09 h^{-1} × 41 mmol-C/g-DW = 3.7 mmol-CO_2/g-DW/h.

3.3. Comparison to optimal flux map

The resulting flux map was compared to a previously published linear programming (LP) solution that predicts the theoretical optimum flux profile that simultaneously maximizes biomass production and minimizes light utilization based on a specified CO_2 uptake rate (Shastri and Morgan, 2005). Table II compares each reaction that exhibited a statistically significant deviation between MFA-determined and LP-predicted flux values. Overall, the INST-MFA results indicate that PA-grown *Synechocystis* cells exhibited suboptimal carbon efficiency, with significant loss of fixed carbon via the oxidative pentose phosphate (OPP) pathway. LP predicts that 111 moles of CO_2 are fixed by RuBisCO (RBC) for every 100 moles of carbon converted to biomass, the difference being due to flux through pyruvate dehydrogenase (PDH), isocitrate dehydrogenase (ICD) and other CO_2-releasing reactions that are necessary to generate biosynthetic precursors. INST-MFA finds that, in actuality, RBC fixed 127 ± 2 moles of CO_2 for every 100 C-moles of biomass produced and released 16 ± 2 moles of fixed CO_2 via the OPP pathway. A significant malic enzyme (ME) flux of 5.3 ± 0.8 moles per 100 C-moles biomass was also identified by INST-MFA, providing an alternate route of pyruvate formation (phosphoenolpyruvate → oxaloacetate → malate → pyruvate) that bypasses the ATP-generating pyruvate kinase (PK) reaction and closely resembles the pathway of carbon fixation found in C4 plants (Hatch, 1987). However, this cycle does not directly contribute to carbon loss since it involves concerted uptake and release of CO_2 by PEP carboxylase (PPC) and ME enzymes acting in tandem, resulting in no net effect on the carbon balance.

3.4. Oxidative pentose phosphate pathway flux

In most organisms, NADP-linked dehydrogenases such as those involved in the OPP pathway serve a predominantly anabolic role by providing reductant and intermediates for biosynthetic processes (Pelroy et al., 1972). However, cyanobacteria use NADPH as a key source of electrons for oxidative phosphorylation in the dark, which is necessary to produce ATP from NADP-linked oxidation of stored glycogen or exogenous glucose (Biggins, 1969). The coupling of NADPH production to oxidative phosphorylation represents a unique respiratory pathway found in few other organisms and is believed to compensate for the lack of an intact cyanobacterial TCA cycle (Pelroy et al., 1972). A previous MFA study reported that over 90% of glucose consumed by *Synechocystis* was oxidized through the OPP pathway under HT conditions (Yang et al., 2002). Our finding that residual levels of OPP pathway flux persist even under PA conditions was unexpected in view of the substantial amounts of NADPH produced by light-driven electron transport. This could indicate incomplete suppression of OPP flux by regulatory circuits that control the transition from dark to light metabolism or, alternatively, the presence of kinetic bottlenecks in the CBB cycle that are circumvented by OPP pathway activation under high-CO_2 conditions.

Knockout mutants of the cyanobacterium species *Synechococcus* sp. PCC 7942 lacking either of the two OPP pathway enzymes glucose-6-phosphate dehydrogenase (G6PD) or 6-phosphogluconate (6PGD) exhibit no significant decrease in growth rate under PA conditions, indicating that OPP pathway activity is dispensable in the light (Broedel and Wolf, 1990; Scanlan et al., 1995). However, prior studies have reported no reduction in enzymatic activity of G6PD or 6PGD in *Synechocystis* cell extracts collected under PA conditions relative to MT or HT conditions (Knowles and Plaxton, 2003) or after shifting cells from light to dark (Singh and Sherman, 2005), suggesting that these key OPP pathway enzymes are highly expressed under PA conditions and are primarily regulated at the posttranslational level. Indeed, it is well known that G6PD controls carbon entry into the OPP pathway and is competitively inhibited by NADPH and allosterically deactivated by reduced thioredoxin in the light (Buchanan, 1991; Grossman and McGowan, 1975; Pelroy et al., 1976a). However, this response is apparently incomplete under the conditions of our

study, which leads to a small but significant CO_2 loss amounting to ~13% of total fixed carbon and a concomitant reduction in photosynthetic efficiency.

3.5. Malic enzyme flux

Our results are in agreement with a previous ^{13}C-MFA study that also reported substantial ME flux in *Synechocystis* under HT and MT growth conditions (Yang et al., 2002). Interestingly, a previously reported *Synechocystis* knockout mutant lacking NADP-dependent malic enzyme grew about 15 times slower than its wild-type parent when grown in continuous light, which provides indirect evidence that ME is expressed and active under the conditions of our study and that ME flux provides a functional benefit to PA growth (Bricker et al., 2004). Because supplementation of pyruvate in the culture medium was able to completely restore PA growth of this knockout strain, the authors concluded that ME flux is required to supply pyruvate for biosynthetic processes due to down-regulation of PK activity in the light. This hypothesis might also explain the presence of ME flux in our system, which effectively bypasses the PK reaction step. Alternatively, Yang et al.(2002) have suggested that this pathway could be involved in the capture and concentration of intracellular CO_2 by cyanobacteria via a process analogous to that observed in C4 plants.

3.6. Cofactor balance

In addition to the direct impact on intracellular carbon flows, the presence of nonzero OPP and ME pathway fluxes also alters the balance of reduced NADPH and NADH cofactors and increases the ATP demand relative to the LP prediction (Table II). Both OPP and ME pathways are coupled to production of the reduced cofactor NADPH in *Synechocystis* (Bricker et al., 2004; Knowles and Plaxton, 2003), although NADPH production in the OPP pathway is completely offset by its consumption in the CBB cycle and therefore has no net effect on NADPH availability. OPP pathway activity indirectly causes a substantial increase in ATP demand due to increased CBB cycling through the ATP-consuming reactions phosphoglycerate kinase (PGK) and phosphoribulokinase (PRK) reactions. This ATP drain is further compounded by ME pathway activity, which converts NADH to NADPH at the expense of ATP. The increased demands for NADPH and ATP are ultimately met by photosynthetic electron transport. Based on the reaction network and assumptions used by Shastri and Morgan (2005) to compute their LP solution, the minimum photosynthetic flux increases from 1297 to 1419 photons per C-mole biomass formed due to the presence of nonzero OPP and ME pathway activities, which represents a 9% loss of energetic efficiency.

3.7. Photorespiration

In contrast to the significant carbon and energetic losses attributable to OPP and ME pathway activities, the INST-MFA results indicate negligible photorespiration. The oxygenase side reaction of RuBisCO exhibited a net flux of 0.4 ± 0.2 moles of 2-phosphoglycolate (2PG) produced per 100 C-moles biomass formed, which was subsequently converted to 3-phosphoglycerate (3PGA) via photorespiration (Fig. 4). This meager flux confirms the presence of an efficient carbon concentrating mechanism in cyanobacteria, which functions to elevate the local concentration of CO_2 in close proximity to RuBisCO and thereby compensate for its low affinity for CO_2 (Kaplan and Reinhold, 1999). In addition, the high concentration of bicarbonate supplied during the carbon labeling experiment would have further suppressed photorespiration under the conditions of our study (Huege et al., 2011). Eisenhut et al. (2008) have shown that blocking photorespiration in *Synechocystis* leads to a high-CO_2-requiring phenotype, and that these mutants accumulated intracellular glycolate even in the presence of 5% CO_2. Our work demonstrates that flux through photorespiration is quantitatively very small compared to the total rate of CO_2 fixation under high-CO_2 conditions. This result is not necessarily inconsistent with the findings of Eisenhut et al., however, since complete removal of photorespiratory pathways

would be expected to cause gradual accumulation of glycolate, even in the presence of low oxygenase activity.

Photorespiratory 2PG metabolism comprises three alternative pathways in *Synechocystis*: (i) a plant-like C2 cycle, (ii) a bacterial glycerate pathway, and (iii) complete decarboxylation of glyoxylate via oxalate (Eisenhut et al., 2008; Hagemann et al., 2010). Flux carried by either of the first two pathways is readily detectable in the measured labeling patterns of glycerate, 3PGA, and PEP (Fig. 5A). However, the C2 cycle and glycerate pathways cannot be distinguished based on these measurements alone, since both produce identical carbon rearrangements as flux proceeds through the non-overlapping reaction steps connecting glyoxylate to glycerate. Although we analyzed isotope labeling in serine and glycine (which are intermediates in the C2 cycle but not the glycerate pathway), these measurements were not precise enough to be included in the flux analysis due to low signal intensities. Therefore, pathways (i) and (ii) were lumped into a single photorespiratory pathway that represents carbon recycling from 2PG to 3PGA and had a net flux of 0.3 ± 0.1 moles per 100 C-moles biomass under the conditions of our study (Fig. 4). The decarboxylation pathway flux could not be accurately quantified using the available isotopomer measurements and was therefore neglected. However, we found that oxalate achieved a maximum average ^{13}C enrichment of approximately 10% even after 20+ minutes of labeling (not shown). Therefore, we concluded that decarboxylation of glyoxylate was likely insignificant under the conditions of our study.

Based on their large-scale *in silico* reconstruction of the *Synechocystis* metabolic network, Knoop et al. (2010) predicted that a photorespiratory flux of approximately 4% of the total RuBisCO activity is necessary to achieve optimal PA growth. However, this prediction was based on the assumption that *Synechocystis* does not possess a pathway to synthesize serine directly from 3PGA and must therefore use glyoxylate as a precursor for glycine, serine, and cysteine biosynthesis. A corollary of this assumption is that all serine carbon would be derived from glycine, with the amino acid backbone contributed directly from glycine and the hydroxyl carbon indirectly from glycine (C2) via methylene tetrahydrofolate (Fig. 5A). Although the serine and glycine labeling measurements were not considered precise enough to be included in the flux analysis, the ^{13}C enrichment of serine was nonetheless substantially higher than glycine at all sample time points, indicating that serine was synthesized directly from 3PGA rather than by photorespiration via glycine. Fig. 5B depicts the labeling of several CBB and C2 cycle intermediates after approximately 4 minutes of $^{13}CO_2$ labeling. At this time point, both serine fragment ions exhibited considerably higher ^{13}C enrichments than was found in glycine fragment ions. This is consistent with a recent paper by Huege et al. (2011) and would appear to contradict the assumption of Knoop et al.

3.8 Glyoxylate shunt

The INST-MFA flux map indicates absence of glyoxylate shunt activity under PA conditions. Although Yang et al. (2002) reported substantial flux through the glyoxylate shunt under HT and MT conditions, Knoop et al. (2010) could find no biochemical or genetic evidence to support the inclusion of the pathway in their large-scale reconstruction of the *Synechocystis* metabolic network. Shastri and Morgan (2005) included the glyoxylate shunt in their earlier flux balance model, but the resulting LP solution predicted that the pathway should be completely inactivated to achieve optimal PA growth. We also included the glyoxylate shunt in our isotopomer model to facilitate comparisons to the earlier work of Yang et al. (2002) and Shastri and Morgan (2005). However, our results confirm that this pathway is either altogether missing from *Synechocystis* or strongly repressed under PA conditions.

3.9 Pool size estimation

Most prior INST-MFA studies have incorporated direct metabolite pool size measurements into the SSR objective function (Noh et al., 2007; Schaub et al., 2008). This was considered necessary to maximize flux identifiability, due to the fact that the pool sizes appear as additional adjustable parameters in the isotopomer balance equations and must be fitted during the flux estimation procedure (Noh and Wiechert, 2006). However, our results indicate that precise flux determination can be achieved using INST-MFA even in the absence of direct pool size measurements. This provides a distinct advantage, since intracellular concentration measurements are easily corrupted by metabolite losses that can occur during sample quenching and extraction. These same losses, however, would not be expected to impact the labeling measurements so long as sufficient material remains for mass isotopomer analysis. We hypothesize that the reason we can achieve good flux identifiability without measuring pool sizes is because the feasible labeling patterns that can occur at convergent nodes in the metabolic network are mostly determined by the atom rearrangements and relative fluxes of the tributary pathways that feed into those nodes. Therefore, by simultaneously fitting mass isotopomer measurements derived from metabolites both upstream and downstream of such nodes, one can adequately constrain the resulting flux estimates to narrow confidence regions. While the pool size parameters serve to match the labeling dynamics of adjacent pools and account for any lags in the network, they cannot drastically alter the isotopomer patterns that emerge within the network once an acceptable flux distribution has been identified.

On the other hand, it is clear from our results that most pool size parameters remain unidentifiable without including direct pool size measurements in the fitting routine (Supplementary Table V). This is to be expected, since many of the pools are close to quasi-equilibrium with respect to surrounding metabolites in the network, and therefore only an upper bound can be estimated for these pool sizes. Also, if there are several intermediate pools separating measurable upstream and downstream metabolites, a delay in the dynamic response of the downstream metabolites could be attributable to any one of the intervening pools. This redundancy will inevitably lead to poor identifiability of pool sizes. As a result of these issues, only a handful of pool sizes could be estimated with both finite upper and nonzero lower bounds (citrate, fructose-1,6-bisphosphate, fumarate, malate, PEP, and succinate). While the estimated values for these pool sizes are within the correct order of magnitude based on prior measurements (Shastri and Morgan, 2007), it is important to note that if a metabolite is in rapid exchange with other metabolites not represented in the isotopomer model, the estimated values will reflect the size of the combined pool. This complicates direct comparisons to experimental concentration measurements.

3.10 Metabolic channeling

Although the steady-state isotope labeling measurements are not directly useful for flux analysis, they do provide information on subcellular compartmentation and metabolic channeling. After correcting for natural isotope abundances, PEP and 3PGA exhibited the highest steady-state ^{13}C-enrichments of 47% and 46%, respectively. Huege et al. (2011) reported significantly higher PEP enrichments compared to 3PGA throughout their labeling period, which they attributed to metabolic channeling of carboxysomal 3PGA into PEP. We also noted slightly higher PEP enrichments in all samples collected after 1 minute of $^{13}CO_2$ labeling, but the differences were typically less than 1 mol% and were not substantial enough to warrant special treatment in our isotopomer model. On the other hand, the CBB cycle intermediates fructose-6-phosphate (F6P), glyceraldehyde-3-phosphate (GAP), dihydroxyacetone phosphate (DHAP), and ribose-5-phosphate (R5P) were significantly less labeled than their downstream products sedoheptulose-7-phosphate (S7P), ribulose-5-phosphate (RU5P), and ribulose-1,5-bisphosphate (RUBP) (Fig. 6). This implies the

presence of metabolic channeling that can arise due to the formation of multienzyme complexes that transfer intermediates directly between catalytic sites without diffusion into the bulk phase of the cell. We estimated the contribution of metabolic channeling by including “dilution parameters” for F6P, GAP, DHAP, and R5P in our isotopomer model. The values obtained from INST-MFA suggest that approximately 10% of the total intracellular concentrations of these intermediates were metabolically inactive and therefore remained unlabeled at steady state. Although the organization of CBB cycle enzymes into multienzyme complexes has been previously reported to occur in plants and green algae (Gontero et al., 1988; Winkel, 2004), our results along with those of Huege et al. appear to provide the first evidence of metabolic channeling in the CBB cycle of cyanobacteria.

4. CONCLUSION

Overall, we were able to precisely quantify the rates of all CBB cycle reactions, as well as several “wasteful” side reactions including G6PD, ME, and photorespiratory fluxes which contribute to suboptimal PA growth of *Synechocystis*. Although earlier studies have applied dynamic isotope labeling experiments to obtain important information about *in vivo* kinetics of CBB cycle reactions (Pelroy et al., 1976b) and photorespiration (Huege et al., 2011) in cyanobacteria, these approaches were not capable of integrating numerous isotopic measurements into a comprehensive flux map that encompasses all major pathways of central carbon metabolism. Furthermore, because these studies did not apply the INST-MFA approach, it was impossible to estimate fluxes without simultaneously measuring the intracellular pool sizes of the labeled intermediates. We have shown that application of INST-MFA in combination with GC-MS and LC-MS/MS analysis of isotope labeling trajectories can effectively quantify photoautotrophic fluxes in cultured cyanobacteria to a high degree of precision. This is possible even in the absence of direct measurements of intracellular pool sizes, which are treated as additional adjustable parameters in the isotopomer model.

Our study provides an example of how flux analysis can be used to identify pathways responsible for reduced cyanobacterial productivity, by pinpointing reactions that contribute to carbon and energetic losses. By determining how these losses are altered by genetic manipulations or by modulation of environmental conditions, we expect that INST-MFA can be a powerful approach for identifying metabolic engineering strategies to improve photosynthetic efficiency or re-route metabolic fluxes to desirable end products in these hosts. Furthermore, INST-MFA is not limited to photosynthetic bacteria, but can be extended to algae, plants, and other microorganisms that grow exclusively on C1 compounds. As a result, the integration of quantitative INST-MFA flux maps with gene expression and proteomic datasets is expected to fill a critical gap in our ability to assess network-wide regulation of carbon and energy flows in photosynthetic organisms.

HIGHLIGHTS

- Isotopically nonstationary metabolic flux analysis (INST-MFA) was applied to map intracellular fluxes in a photoautotroph (*Synechocystis* sp. PCC6803) for the first time.
- Inefficiencies in photosynthesis were discovered due to oxidative pentose phosphate pathway and malic enzyme activity.
- Recycling of 2-phosphoglycolate to 3-phosphoglycerate was negligible under the high-CO_2 conditions of our study.
- This approach can be applied to map fluxes in cyanobacteria, algae, and plants.

Supplementary Material

Refer to Web version on PubMed Central for supplementary material.

ABBREVIATIONS

2PG	2-phosphoglycolate
2PGA	2-phosphoglycerate
3PGA	3-phosphoglycerate
6PGD	6-phosphogluconate dehydrogenase
ACA	acetyl-CoA
AGT	alanine/glyoxylate aminotransferase
AKG	alpha-ketoglutarate
CIT	citrate
CS	citrate synthase
DHAP	dihydroxyacetone phosphate
E4P	erythrose 4-phosphate
EC2	transketolase-bound 2-carbon fragment
EC3	transaldolase-bound 3-carbon fragment
EMU	elementary metabolite unit
ENO	enolase
F6P	fructose-6-phosphate
FBA	fructose bisphosphate aldolase
FBP	fructose 1,6-bisphosphate
FDH	formate dehydrogenase
FOR	formate
FUM	fumarate
FUS	fumarase
G6P	glucose 6-phosphate
G6PD	glucose-6-phosphate dehydrogenase
GA	glycerate
GAP	glyceraldehyde 3-phosphate
GAPDH	glyceraldehyde-3-phosphate dehydrogenase
GCL	glyoxylate carboligase
GC-MS	gas chromatography-mass spectrometry
GDC	glycine decarboxylase
GGT	glycine/glutamate aminotransferase
GLC	glycolate
GLD	glycolate dehydrogenase

GLY	glycine
GLYC	glycogen
GLYK	glycerate kinase
GOX	glyoxylate
GXO	glyoxylate oxidase
HPA	hydroxypyruvate
HPR	hydroxypyruvate reductase
ICD	isocitrate dehydrogenase
ICI	isocitrate
ICL	isocitrate lyase
INST-MFA	isotopically nonstationary metabolic flux analysis
LB	lower bound
LC-MS/MS	liquid chromatography-tandem mass spectrometry
LP	linear programming
MAL	malate
MDH	malate dehydrogenase
MFA	metabolic flux analysis
ME	malic enzyme
MID	mass isotopomer distribution
MRM	multiple reaction monitoring
MS	malate synthase
MTHF	5,10-methylenetetrahydrofolate
OAA	oxaloacetate
ODC	oxalate decarboxylase
ODE	ordinary differential equation
OPP	oxidative pentose phosphate
P5P	pentose-5-phosphate
PDH	pyruvate dehydrogenase
PEP	phosphoenolpyruvate
PGI	phosphoglucose isomerase
PGK	phosphoglycerate kinase
PGM	phosphoglycerate mutase
PGP	phosphoglycolate phosphatase
PK	pyruvate kinase
PPC	phosphoenolpyruvate carboxylase
PPE	phosphopentose epimerase

PPI	phosphopentose isomerase
PRK	phosphoribulokinase
PYR	pyruvate
R5P	ribose-5-phosphate
RBC	ribulose-1,5-bisphosphate carboxylase oxygenase (RuBisCO)
RU5P	ribulose-5-phosphate
RUBP	ribulose-1,5-bisphosphate
S7P	sedoheptulose-7-phosphate
SBA	sedoheptulose-1,7-bisphosphate aldolase
SBP	sedoheptulose-1,7-bisphosphate
SER	serine
SHMT	serine hydroxymethyltransferase
SSR	sum-of-squared residuals
SUC	succinate
TAL	transaldolase
TCA	tricarboxylic acid
THF	tetrahydrofolate
TKT	transketolase
TSA	tartronic semialdehyde
TSR	tartronic semialdehyde reductase
UB	upper bound
X5P	xylulose 5-phosphate

Acknowledgments

This work was supported by NSF BES 0348458 (to JAM), NIH R01 DK075850 (to GS) and NIH F32 DK072856 (to JDY).

REFERENCES

Antoniewicz MR, Kelleher JK, Stephanopoulos G. Determination of confidence intervals of metabolic fluxes estimated from stable isotope measurements. Metab Eng. 2006; 8:324–337. [PubMed: 16631402]

Antoniewicz MR, Kelleher JK, Stephanopoulos G. Elementary metabolite units (EMU): a novel framework for modeling isotopic distributions. Metab Eng. 2007; 9:68–86. [PubMed: 17088092]

Atsumi S, Higashide W, Liao JC. Direct photosynthetic recycling of carbon dioxide to isobutyraldehyde. Nat Biotechnol. 2009; 27:1177–1180. [PubMed: 19915552]

Berg IA, Kockelkorn D, Ramos-Vera WH, Say RF, Zarzycki J, Hugler M, Alber BE, Fuchs G. Autotrophic carbon fixation in archaea. Nat Rev Microbiol. 2010; 8:447–460. [PubMed: 20453874]

Biggins J. Respiration in blue-green algae. Journal of Bacteriology. 1969; 99:570–575. [PubMed: 4390093]

Bricker TM, Zhang S, Laborde SM, Mayer PR 3rd, Frankel LK, Moroney JV. The malic enzyme is required for optimal photoautotrophic growth of Synechocystis sp. strain PCC 6803 under

continuous light but not under a diurnal light regimen. Journal of Bacteriology. 2004; 186:8144–8148. [PubMed: 15547288]

Broedel SE Jr, Wolf RE Jr. Genetic tagging, cloning, and DNA sequence of the Synechococcus sp. strain PCC 7942 gene (gnd) encoding 6-phosphogluconate dehydrogenase. Journal of Bacteriology. 1990; 172:4023–4031. [PubMed: 2113917]

Buchanan BB. Regulation of CO2 assimilation in oxygenic photosynthesis: the ferredoxin/thioredoxin system. Perspective on its discovery, present status, and future development. Archives of Biochemistry and Biophysics. 1991; 288:1–9. [PubMed: 1910303]

Dutta D, De D, Chaudhuri S, Bhattacharya SK. Hydrogen production by Cyanobacteria. Microbial Cell Factories. 2005; 4 -.

Eisenhut M, Ruth W, Haimovich M, Bauwe H, Kaplan A, Hagemann M. The photorespiratory glycolate metabolism is essential for cyanobacteria and might have been conveyed endosymbiontically to plants. Proc Natl Acad Sci U S A. 2008; 105:17199–17204. [PubMed: 18957552]

Fernandez CA, Des Rosiers C, Previs SF, David F, Brunengraber H. Correction of 13C mass isotopomer distributions for natural stable isotope abundance. J Mass Spectrom. 1996; 31:255–262. [PubMed: 8799277]

Gontero B, Cardenas ML, Ricard J. A functional five-enzyme complex of chloroplasts involved in the Calvin cycle. Eur J Biochem. 1988; 173:437–443. [PubMed: 2834208]

Grossman A, McGowan RE. Regulation of glucose 6-phosphate dehydrogenase in blue-green algae. Plant Physiology. 1975; 55:658–662. [PubMed: 16659143]

Hagemann M, Eisenhut M, Hackenberg C, Bauwe H. Pathway and importance of photorespiratory 2-phosphoglycolate metabolism in cyanobacteria. Adv Exp Med Biol. 2010; 675:91–108. [PubMed: 20532737]

Hatch MD. C4 photosynthesis: a unique elend of modified biochemistry, anatomy and ultrastructure. Biochimica et Biophysica Acta (BBA) - Reviews on Bioenergetics. 1987; 895:81–106.

Huege J, Goetze J, Schwarz D, Bauwe H, Hagemann M, Kopka J. Modulation of the major paths of carbon in photorespiratory mutants of synechocystis. PLoS One. 2011; 6:e16278. [PubMed: 21283704]

Huege J, Sulpice R, Gibon Y, Lisec J, Koehl K, Kopka J. GC-EI-TOF-MS analysis of in vivo carbon-partitioning into soluble metabolite pools of higher plants by monitoring isotope dilution after 13CO2 labelling. Phytochemistry. 2007; 68:2258–2272. [PubMed: 17475294]

Kaplan A, Reinhold L. CO_2 Concentrating Mechanisms in Photosynthetic Microorganisms. Annu Rev Plant Physiol Plant Mol Biol. 1999; 50:539–570. [PubMed: 15012219]

Kitson, FG.; Larsen, BS.; McEwen, CN. Gas chromatography and mass spectrometry : a practical guide. San Diego: Academic Press; 1996.

Knoop H, Zilliges Y, Lockau W, Steuer R. The metabolic network of Synechocystis sp. PCC 6803: systemic properties of autotrophic growth. Plant Physiology. 2010; 154:410–422. [PubMed: 20616194]

Knowles VL, Plaxton WC. From genome to enzyme: analysis of key glycolytic and oxidative pentose-phosphate pathway enzymes in the cyanobacterium Synechocystis sp. PCC 6803. Plant and Cell Physiology. 2003; 44:758–763. [PubMed: 12881504]

Lindberg P, Park S, Melis A. Engineering a platform for photosynthetic isoprene production in cyanobacteria, using Synechocystis as the model organism. Metab Eng. 2010; 12:70–79. [PubMed: 19833224]

Liu X, Sheng J, Curtiss R Iii. Fatty acid production in genetically modified cyanobacteria. Proc Natl Acad Sci U S A. 2011

Luo B, Groenke K, Takors R, Wandrey C, Oldiges M. Simultaneous determination of multiple intracellular metabolites in glycolysis, pentose phosphate pathway and tricarboxylic acid cycle by liquid chromatography-mass spectrometry. J Chromatogr A. 2007; 1147:153–164. [PubMed: 17376459]

Madsen, K.; Nielsen, HB.; Tingleff, O. Methods for non-linear least squares problems. 2nd edition. Lecture notes, Technical University of Denmark; 2004.

Mollney M, Wiechert W, Kownatzki D, de Graaf AA. Bidirectional reaction steps in metabolic networks: IV. Optimal design of isotopomer labeling experiments. Biotechnol Bioeng. 1999; 66:86–103. [PubMed: 10567067]

Noh K, Gronke K, Luo B, Takors R, Oldiges M, Wiechert W. Metabolic flux analysis at ultra short time scale: isotopically non-stationary 13C labeling experiments. Journal of Biotechnology. 2007; 129:249–267. [PubMed: 17207877]

Noh K, Wiechert W. Experimental design principles for isotopically instationary ^{13}C labeling experiments. Biotechnology and Bioengineering. 2006; 94:234–251. [PubMed: 16598793]

Oldiges M, Kunze M, Degenring D, Sprenger GA, Takors R. Stimulation, monitoring, and analysis of pathway dynamics by metabolic profiling in the aromatic amino acid pathway. Biotechnology Progress. 2004; 20:1623–1633. [PubMed: 15575692]

Overmann, J.; Garcia-Pichel, F. The Phototrophic Way of Life. In: Dworkin, M.; Falkow, S., editors. The prokaryotes: A handbook on the biology of bacteria. Vol. vol. 2. New York ; London: Springer; 2006. p. 32-85.

Pelroy RA, Kirk MR, Bassham JA. Photosystem II regulation of macromolecule synthesis in the blue-green alga Aphanocapsa 6714. Journal of Bacteriology. 1976a; 128:623–632. [PubMed: 10279]

Pelroy RA, Levine GA, Bassham JA. Kinetics of light-dark CO2 fixation and glucose assimilation by Aphanocapsa 6714. Journal of Bacteriology. 1976b; 128:633–643. [PubMed: 185198]

Pelroy RA, Rippka R, Stanier RY. Metabolism of glucose by unicellular blue-green algae. Arch Mikrobiol. 1972; 87:303–322. [PubMed: 4629415]

Petersson G. Mass spectrometry of aldonic and deoxyaldonic acids as trimethylsilyl derivatives. Tetrahedron. 1970; 26:16.

Petersson G. Mass spectrometry of hydroxy dicarboxylic acids as trimethylsilyl derivatives. Rearrangement fragmentations. Organic Mass Spectrometry. 1972; 6:12.

Roessner U, Wagner C, Kopka J, Trethewey RN, Willmitzer L. Simultaneous analysis of metabolites in potato tuber by gas chromatography-mass spectrometry. Plant Journal. 2000; 23:131–142. [PubMed: 10929108]

Sauer U. Metabolic networks in motion: ^{13}C-based flux analysis. Mol Syst Biol. 2006; 2:62. [PubMed: 17102807]

Scanlan DJ, Sundaram S, Newman J, Mann NH, Carr NG. Characterization of a zwf mutant of Synechococcus sp. strain PCC 7942. Journal of Bacteriology. 1995; 177:2550–2553. [PubMed: 7730289]

Schaub J, Mauch K, Reuss M. Metabolic flux analysis in *Escherichia coli* by integrating isotopic dynamic and isotopic stationary ^{13}C labeling data. Biotechnol Bioeng. 2008; 99:1170–1185. [PubMed: 17972325]

Schwender J. Metabolic flux analysis as a tool in metabolic engineering of plants. Curr Opin Biotechnol. 2008; 19:131–137. [PubMed: 18378441]

Shastri AA, Morgan JA. Flux balance analysis of photoautotrophic metabolism. Biotechnology Progress. 2005; 21:1617–1626. [PubMed: 16321043]

Shastri AA, Morgan JA. A transient isotopic labeling methodology for ^{13}C metabolic flux analysis of photoautotrophic microorganisms. Phytochemistry. 2007; 68:2302–2312. [PubMed: 17524438]

Sheehan J. Engineering direct conversion of CO2 to biofuel. Nature Biotechnology. 2009; 27:1128–1129.

Singh AK, Sherman LA. Pleiotropic effect of a histidine kinase on carbohydrate metabolism in Synechocystis sp. strain PCC 6803 and its requirement for heterotrophic growth. Journal of Bacteriology. 2005; 187:2368–2376. [PubMed: 15774880]

Tisza, SaM-P.; Ibolya. GC-MS quantitation of isocitric acid in the presence of a large excess of citric acid. Journal of High Resolution Chromatography. 1994; 17:4.

Wiechert W, Noh K. From stationary to instationary metabolic flux analysis. Adv Biochem Eng Biotechnol. 2005; 92:145–172. [PubMed: 15791936]

Winkel BS. Metabolic channeling in plants. Annu Rev Plant Biol. 2004; 55:85–107. [PubMed: 15725058]

Yang C, Hua Q, Shimizu K. Metabolic flux analysis in Synechocystis using isotope distribution from ^{13}C-labeled glucose. Metab Eng. 2002; 4:202–216. [PubMed: 12616690]

Young JD, Walther JL, Antoniewicz MR, Yoo H, Stephanopoulos G. An elementary metabolite unit (EMU) based method of isotopically nonstationary flux analysis. Biotechnol Bioeng. 2008; 99:686–699. [PubMed: 17787013]

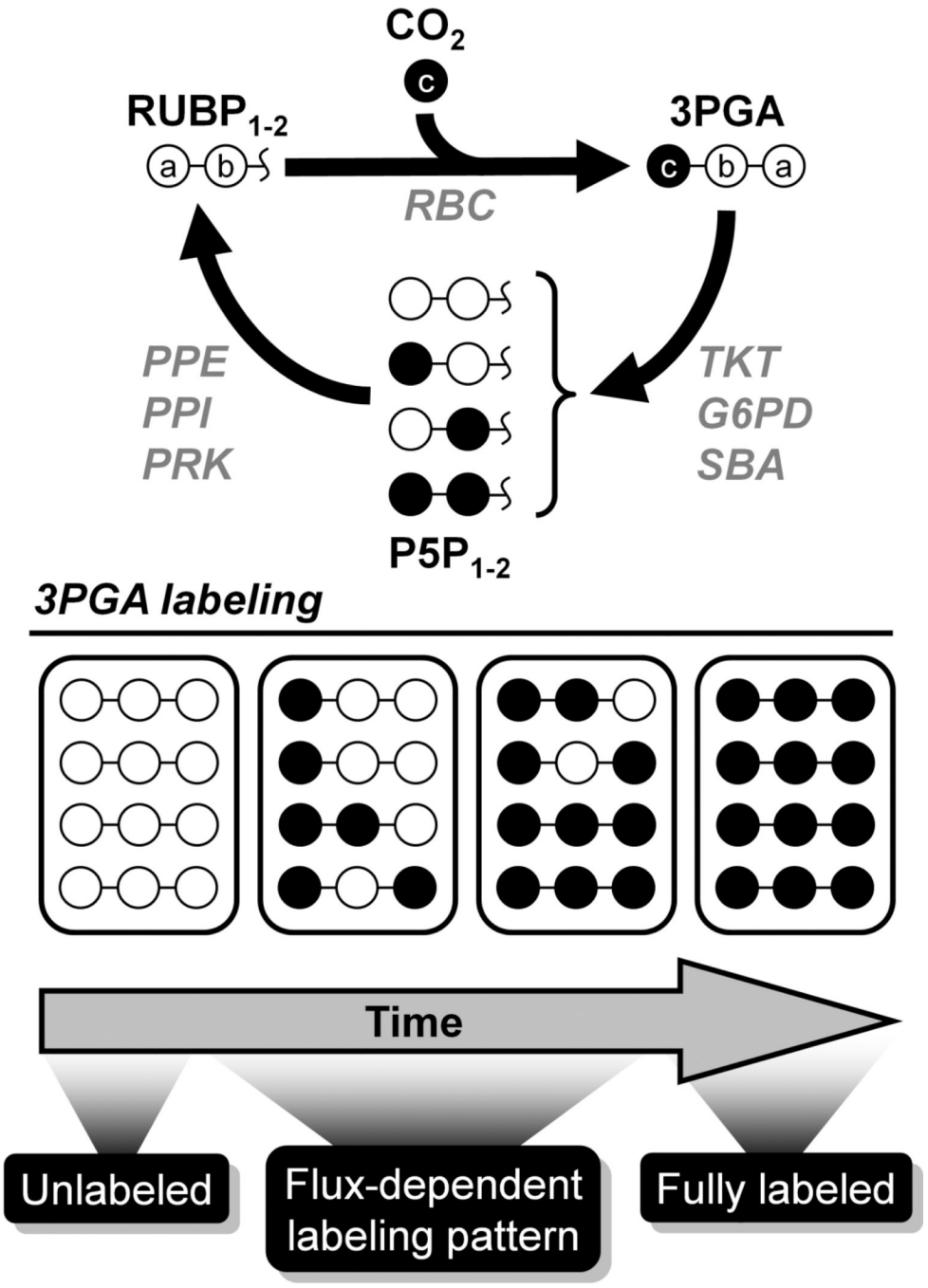

Figure 1. Simplified example of carbon labeling in a photoautotrophic system

Following a switch from natural CO_2 to $^{13}CO_2$, intracellular metabolites become gradually labeled over time. 3-phosphoglycerate (3PGA) becomes ^{13}C-labeled due to carbon fixation by RuBisCO (RBC), resulting in labeling of pentose-5-phosphate (P5P) intermediates of the Calvin-Benson-Bassham (CBB) cycle. Once steady-state labeling is achieved, all metabolites are uniformly ^{13}C-labeled irrespective of fluxes and intracellular pool sizes. Labeling patterns observed during the isotopically transient period, however, can be computationally analyzed to determine fluxes.

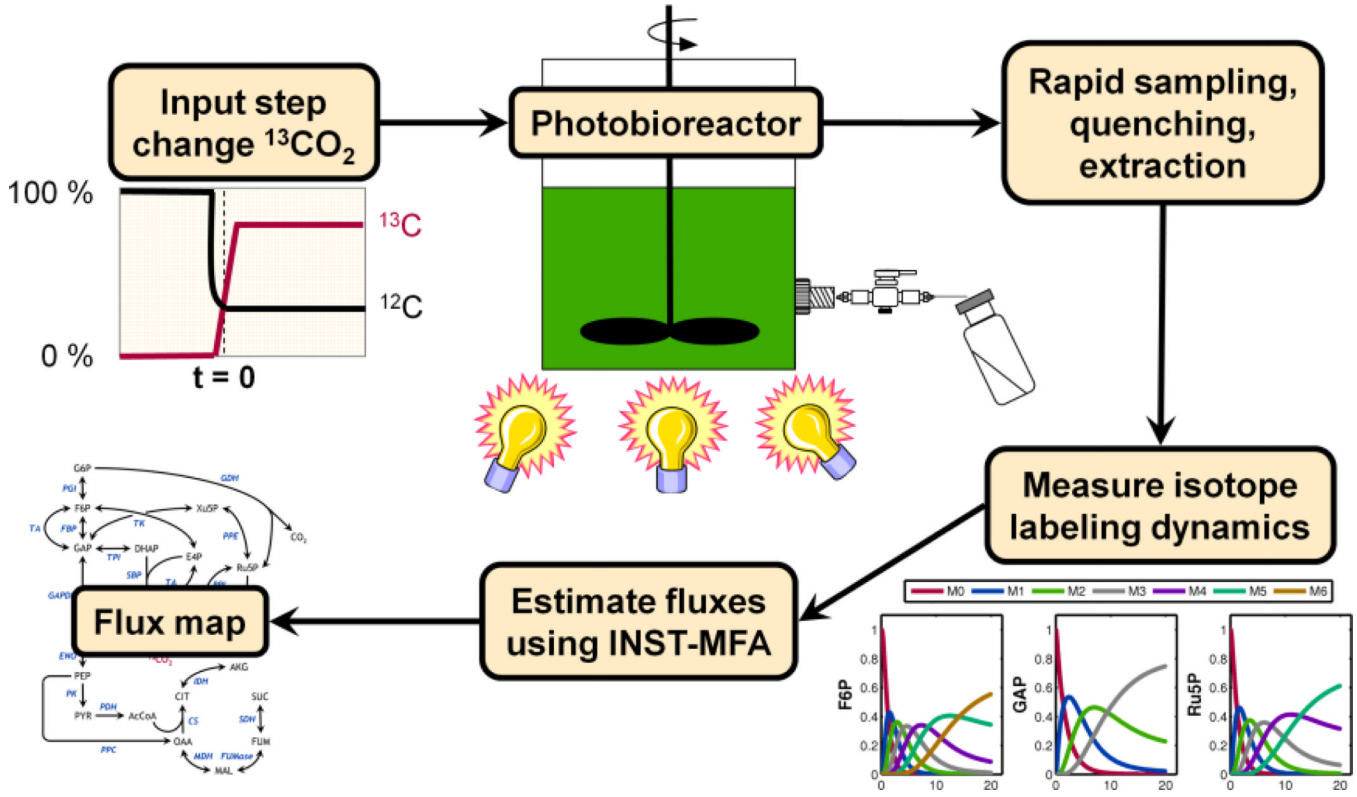

Figure 2. Overview of INST-MFA procedure

Following introduction of ^{13}C-labeled bicarbonate, a series of metabolite samples were obtained by rapid quenching and extraction of cyanobacterial cells. Dynamic changes in isotope labeling patterns were assessed using GC-MS and LC-MS/MS, followed by computational analysis of these trajectories to estimate metabolic pathway fluxes.

3A

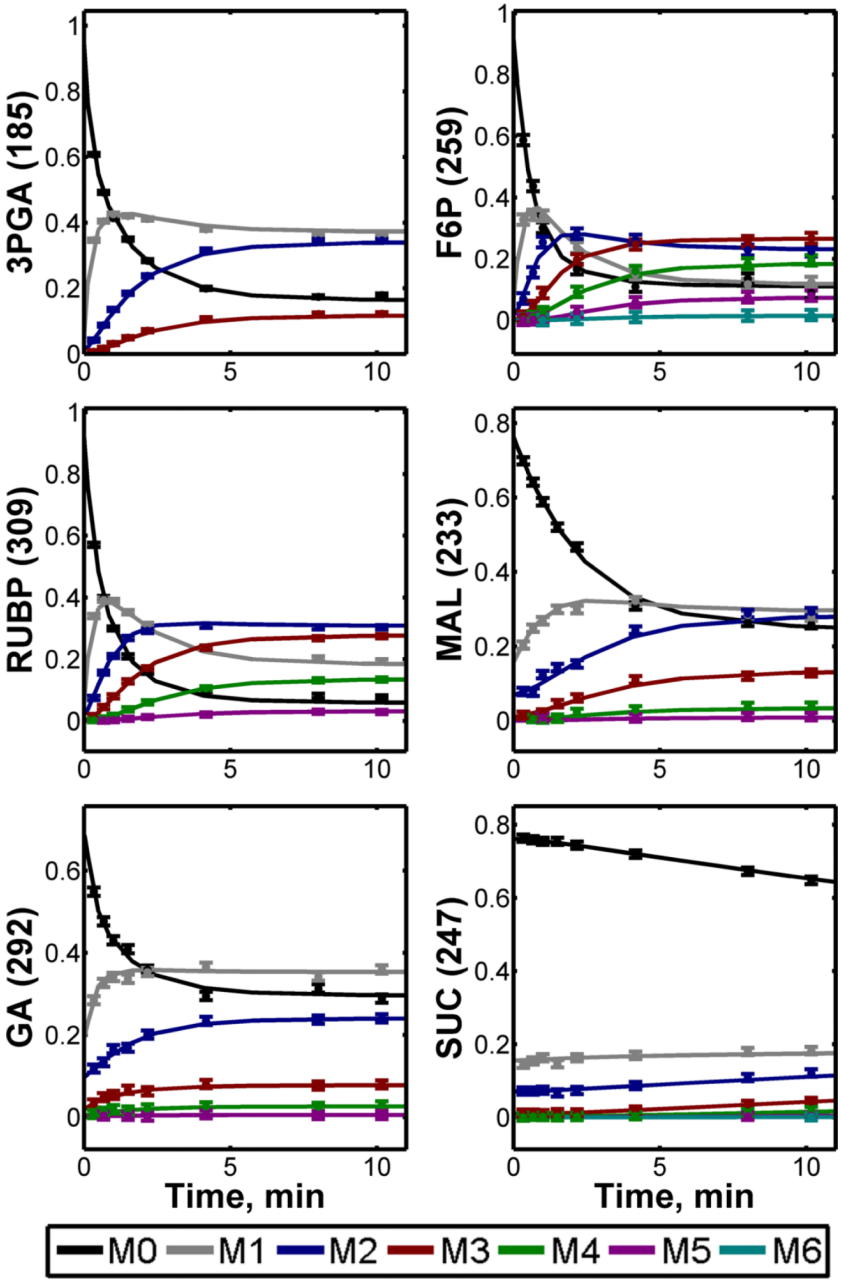

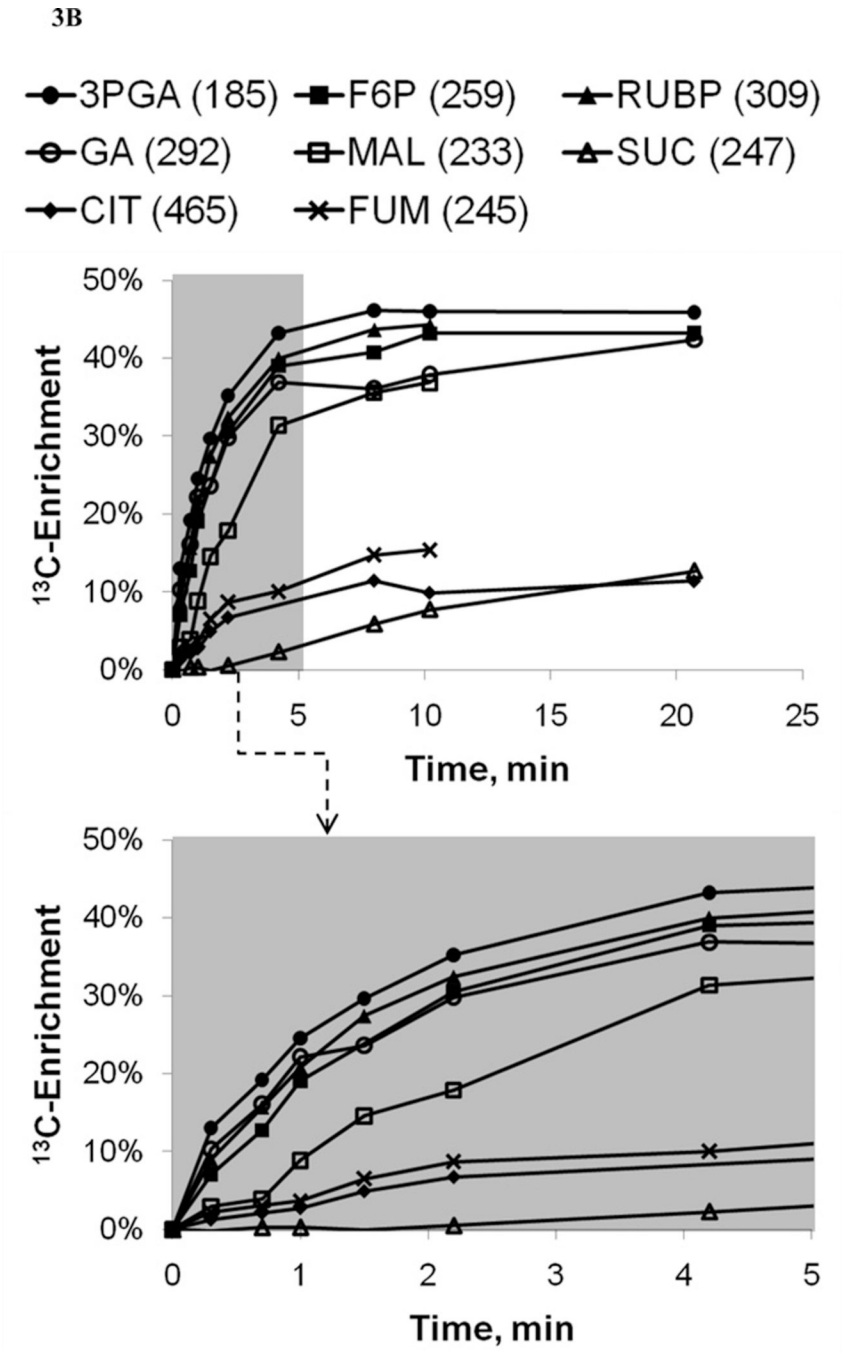

Figure 3. ^{13}C-Labeling trajectories of selected central carbon metabolites

(A) Experimentally measured mass isotopomer abundances (data points) and INST-MFA model fits (solid lines). Error bars represent standard measurement errors. Raw mass isotopomer data are shown without correction for natural isotope abundance. **(B)** Average ^{13}C-enrichments of selected ion fragments. Mass isotopomer distributions were corrected for natural isotope abundance using the method of Fernandez et al. (1996), and average ^{13}C enrichment was calculated using the formula $\frac{1}{N}\sum_{i=1}^{N} Mi \times i$, where N is the number of carbon atoms in the metabolite and Mi is the fractional abundance of the ith mass

isotopomer. The top axis shows the full labeling trajectory and the bottom axis shows an enlarged view of the highlighted region from 0–5 min. Ions shown are for 3-phosphoglycerate (3PGA), fructose-6-phosphate (F6P), ribulose-1,5-bisphosphate (RUBP), malate (MAL), glycerate (GA), succinate (SUC), citrate (CIT) and fumarate (FUM). Nominal masses of M0 mass isotopomers are shown in parentheses.

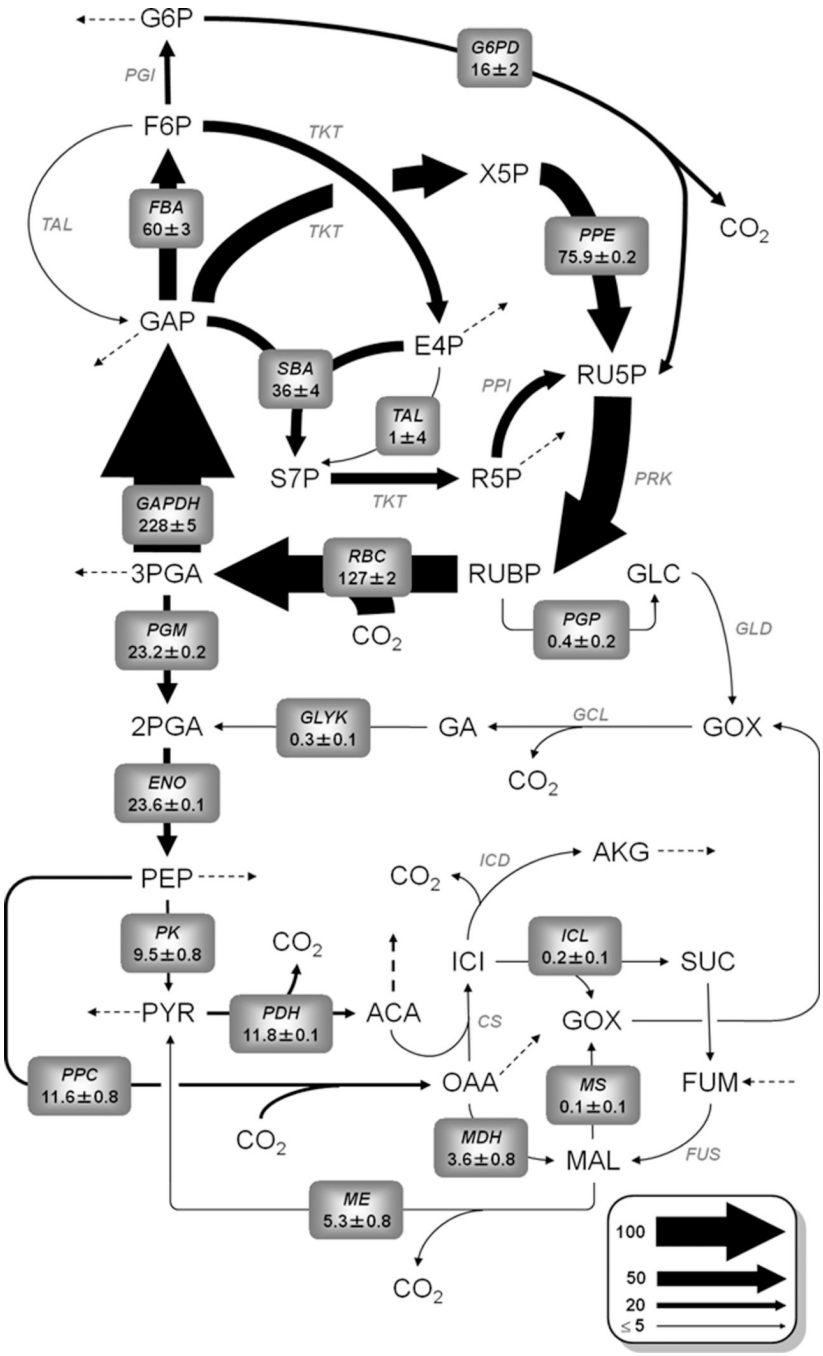

Figure 4. *Synechocystis* flux map determined under photoautotrophic growth conditions

Net fluxes are shown normalized to a net CO_2 uptake rate of 100. Values are represented as $M \pm SE$, where M is the median of the 95% flux confidence interval and SE is the estimated standard error of M calculated as (UB95 – LB95)/3.92. (UB95 and LB95 are the upper and lower bounds of the 95% confidence interval, respectively.) Arrow thickness is scaled proportional to net flux. Dotted arrows indicate fluxes to biomass formation.

5A

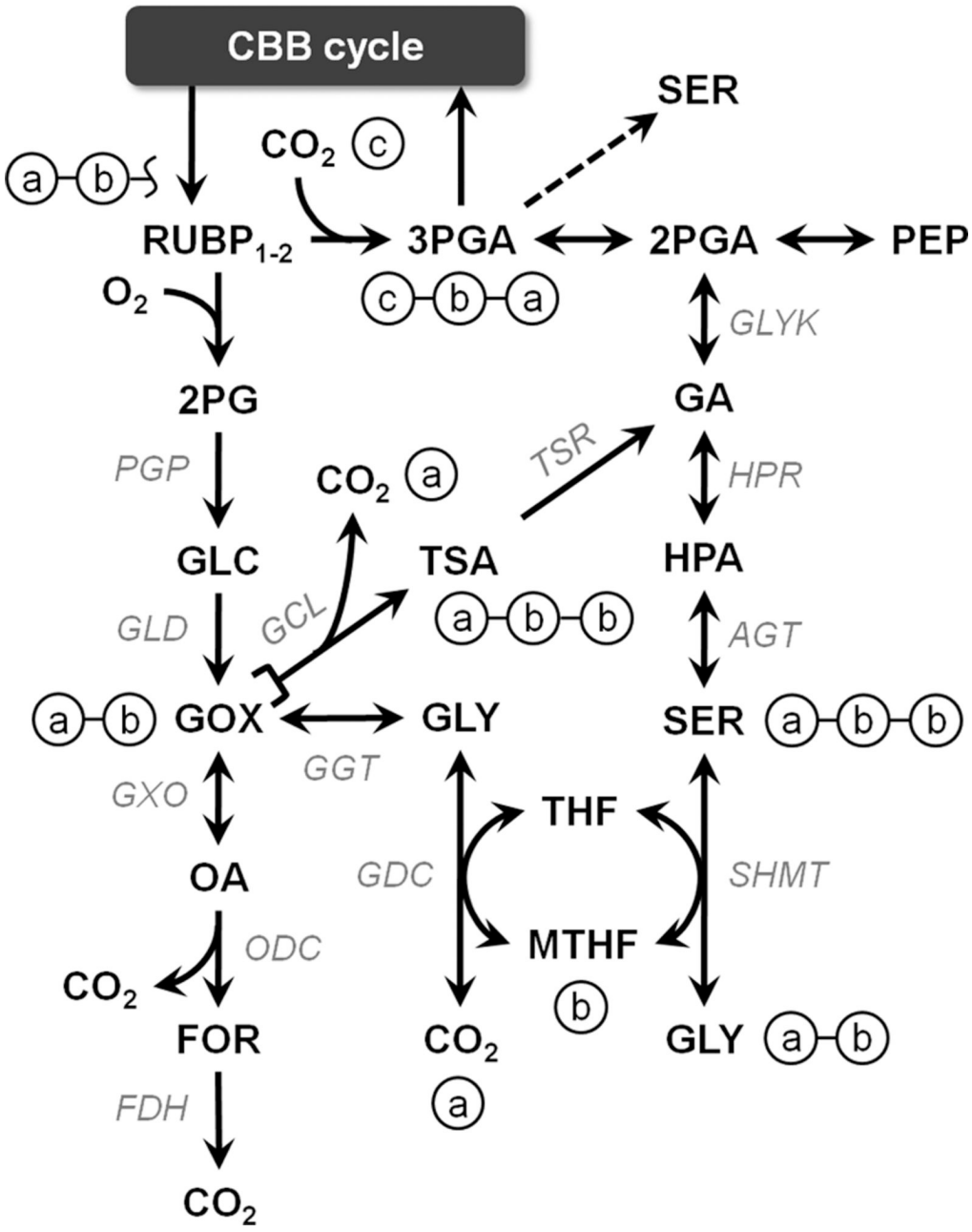

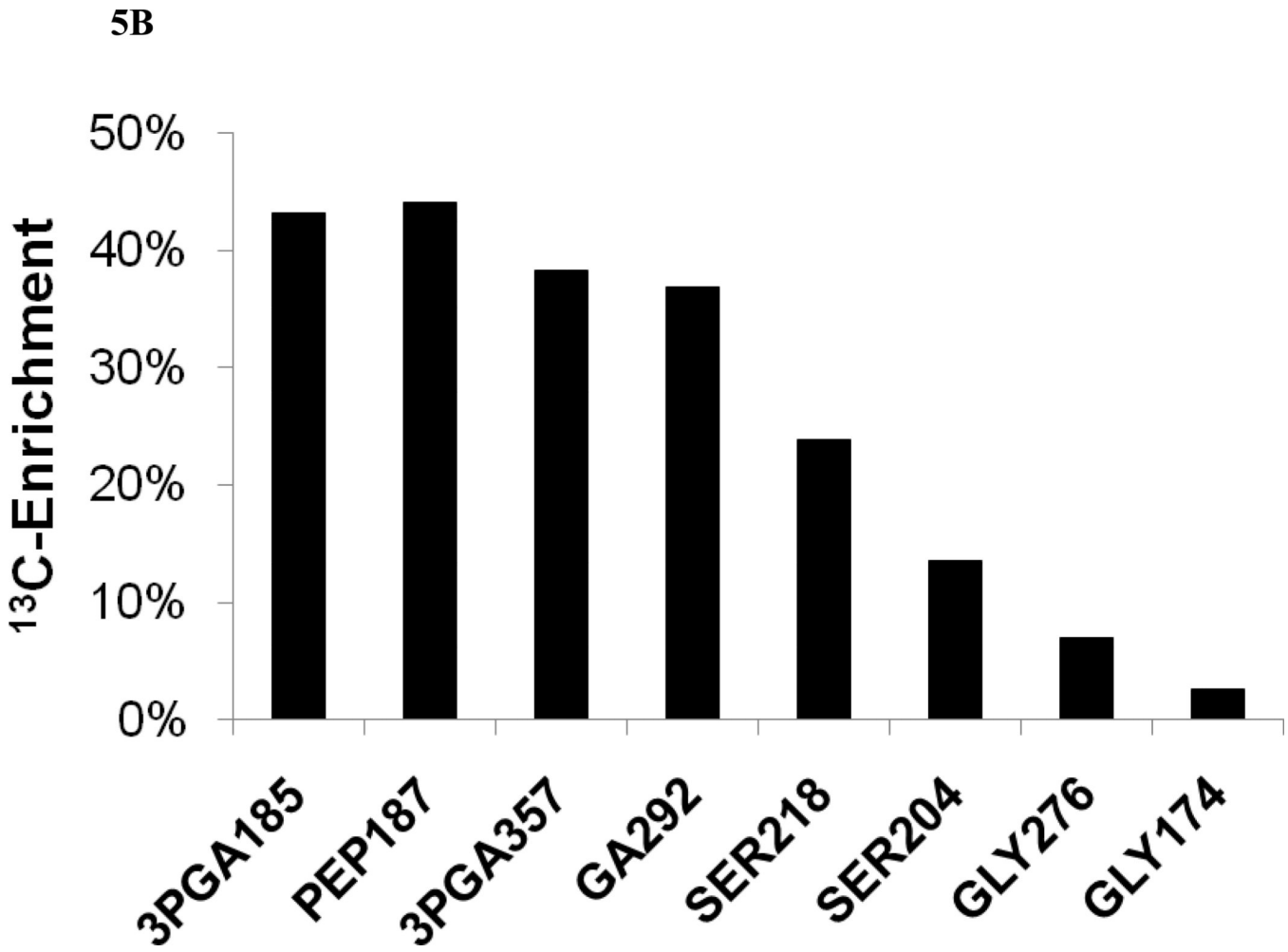

Figure 5. Isotope labeling in photorepiratory pathways

(A) Schematic diagram of the complete 2PG metabolism of *Synechocystis* showing the fate of the first two carbon atoms of ribulose-1,5-bisphosphate. The three photorespiratory pathways diverge at glyoxylate into the plant-like C2 cycle (via glycine and serine), the bacterial-like glycerate pathway (via tartronic semialdehyde), and the decarboxylation branch (via oxalate). The first two pathways re-converge at glycerate. **(B)** ^{13}C enrichments of photorespiratory pathway intermediates after 4.2 minutes of $^{13}CO_2$ labeling. Average enrichments were calculated as described in the caption to Figure 3B. The compositions of selected 3-phosphoglycerate (3PGA), phosphoenolpyruvate (PEP), and glycerate (GA) fragment ions are listed in Table I. The carbon atoms of serine (SER) and glycine (GLY) contained in the selected fragment ions were taken from Huege et al. (2007): SER218 (C1-C2), SER204 (C2-C3), GLY276 (C1-C2), GLY174 (C2).

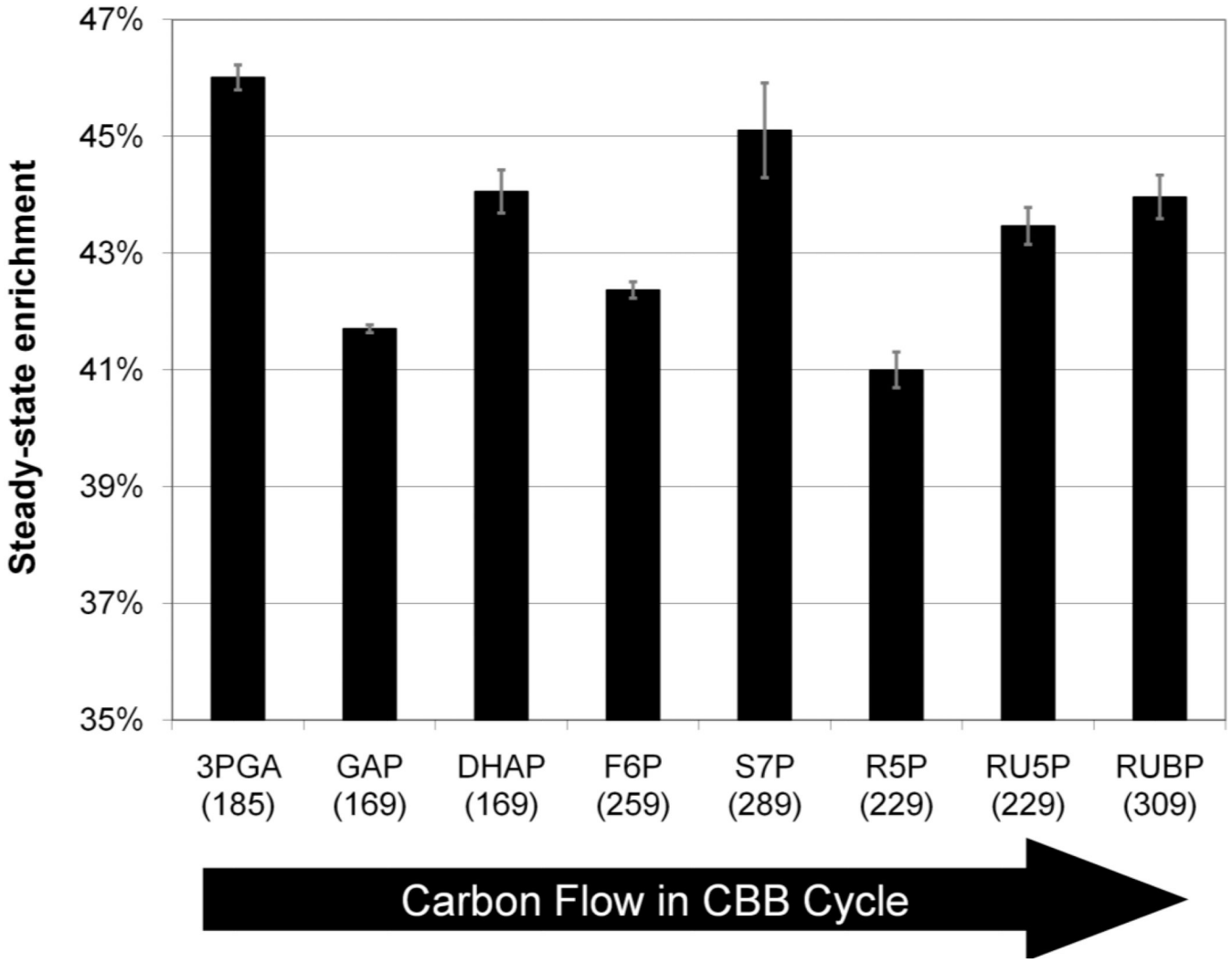

Figure 6. Average steady-state ^{13}C enrichment of CBB cycle intermediates

Average enrichments were calculated as described in the caption to Figure 3B. The labeling of all CBB intermediates achieved steady state at times greater than 8 minutes after tracer administration. Averages of at least two steady-state time points are shown. Error bars indicate standard errors of the mean values.

TABLE I

Isotope labeling measurements used for metabolic flux determination

(a) LC-MS/MS ions and (b) GC-MS ions used to assess metabolite labeling. Standard errors of measurement (SEM) were determined based on the lack of agreement between measured and theoretically computed mass isotopomer distributions obtained from unlabeled cell extracts.

(a) LC-MS/MS ions

Metabolite	*Mass*	*Carbons*	*Composition*	*SEM*	*Reference*
3PGA	185	1-2-3	$C_3H_6O_7P$	0.5	(Luo et al., 2007)
DHAP	169	1-2-3	$C_3H_6O_6P$	1.3	Ibid.
F6P	259	1-2-3-4-5-6	$C_6H_{12}O_9P$	1.7	Ibid.
G6P	259	1-2-3-4-5-6	$C_6H_{12}O_9P$	1.4	Ibid.
GAP	169	1-2-3	$C_3H_6O_6P$	1.3	Ibid.
PEP	167	1-2-3	$C_3H_4O_6P$	0.5	Ibid.
R5P	229	1-2-3-4-5	$C_5H_{10}O_8P$	1.5	Ibid.
RUBP	309	1-2-3-4-5	$C_5H_{11}O_{11}P_2$	0.7	Ibid.
S7P	289	1-2-3-4-5-6-7	$C_7H_{14}O_{10}P$	2.8	Ibid.
RU5P	229	1-2-3-4-5	$C_5H_{10}O_8P$	1.3	Ibid.

(b) GC-MS ions

Metabolite	*Mass*	*Carbons*	*Composition*	*SEM*	*Reference*
3PGA	357	2-3	$C_{11}H_{30}O_5PSi_3$	1.0	(Kitson et al., 1996)
3PGA	459	1-2-3	$C_{14}H_{36}O_7PSi_4$	1.0	Ibid.
CIT	273	1-2-3-4-5	$C_{11}H_{21}O_4Si_2$	1.0	(Tisza, 1994)
CIT	363	1-2-3-4-5	$C_{14}H_{31}O_5Si_3$	1.0	Ibid.
CIT	375	1-2-3-4-5-6	$C_{14}H_{27}O_6Si_3$	1.6	(Huege et al., 2007)
CIT	465	1-2-3-4-5-6	$C_{17}H_{37}O_7Si_4$	1.1	Ibid.
FUM	245	1-2-3-4	$C_9H_{17}O_4Si_2$	1.0	Ibid.
GA	292	1-2	$C_{11}H_{28}O_3Si_3$	1.0	(Petersson, 1970)
GA	307	1-2-3	$C_{11}H_{27}O_4Si_3$	1.3	(Huege et al., 2007)
MAL	233	2-3-4	$C_9H_{21}O_3Si_2$	1.0	(Petersson, 1972)

(a) LC-MS/MS ions

Metabolite	*Mass*	*Carbons*	*Composition*	*SEM*	*Reference*
SUC	247	1-2-3-4	$C_9H_{19}O_4Si_2$	1.0	(Huege et al., 2007)

TABLE II

Reactions that exhibit significant deviation between LP-predicted and MFA-determined fluxes

All fluxes are relative to a net CO_2 uptake rate of 100. The median, lower bound (LB), and upper bound (UB) of the 95% confidence interval is shown for each MFA-determined flux. Grouped fluxes are correlated due to pathway dependencies, and therefore deviations within each group can be attributed to the same underlying feature. Increased OPP pathway flux is responsible for deviations in Group I, while increased ME flux is responsible for deviations in Group II. The three rightmost columns show the net effect of these deviations on the balance of NADPH, NADH and ATP cofactors.

			^{13}C *MFA*			*Cofactor balance*		
Flux	***Reaction***	***LP Predicted***	***Median Value***	***95% LB***	***95% UB***	***NADPH***	***NADH***	***ATP***
Group I								
PGI	F6P → G6P	3	19	15	24			
G6PD/6PGD	G6P → RU5P + CO2 + 2 NADPH	0	16	12	21	+32		
FBA/FBP	DHAP + GAP → F6P	41	60	53	66			
TPI	GAP → DHAP	78	95	90	99			
PGK/GAPDH	3 PGA + ATP + NADPH → GAP	196	228	219	237	−32		−32
PRK	RU5P + ATP → RUBP	111	127	123	132			−16
RBC	RUBP + CO2 → 2 3PGA	111	127	123	132			
Group II								
PK	PEP → PYR + ATP	14.7	9.5	7.9	11.1			−5.2
MDH	OAA + NADH → MAL	−1.7	3.6	1.9	5.2		−5.3	
ME	MAL → PYR + CO2 + NADPH	0	5.3	3.7	6.9	+5.3		
PPC	PEP + CO2 → OAA	6.3	11.6	9.9	13.2			
						Net +5.3	−5.3	−53